Numerical simulation of waves generated by a moving pressure field

D. Bayraktar Ersan*, S. Beji

Faculty of Naval Architecture and Ocean Engineering, Istanbul Technical University, Maslak 34469, Istanbul, Turkey

ARTICLE INFO

ABSTRACT

Boussinesq equations with improved dispersion characteristics are employed to simulate the generation and propagation of waves due to a moving pressure field. The equations with surface pressure terms are discretized in an unconventional way so that the numerical scheme could be run in three different modes: the non-dispersive long wave mode, the classical and the improved Boussinesq mode. For a Gaussian shaped moving pressure field, the analytical solution obtained from the linearized 1-D long wave equations is used for comparisons with the numerical solutions obtained from three different modes of the scheme. A moving hemispherical pressure field and a slender ship-like pressure field are employed for 2-D numerical simulations for a range of Froude numbers. Numerically obtained wedge angles are compared with the values given by the analytical formulas of Havelock. Nonlinear simulations are also performed for visual comparisons with their linear counterparts.

© 2012 Elsevier Ltd. All rights reserved.

1. Introduction

Ocean surface waves, or simply water waves, are mainly generated by wind. However, besides wind generated offshore and near shore waves, waves generated by moving bodies are always of interest. In particular, simulation of wave motions due to ship-like surface vessels in mildly varying bathymetry is the subject matter of the present work. Further extensions to study the transformation of ship wave spectra in strongly varying bottom topography as in Belibassakis (2003), and to examine the wave interactions with other structures are also possible.

The earliest depth-averaged wave equation that included weakly dispersive and nonlinear effects was derived by Boussinesq (1872), in which the non-hydrostatic pressure was approximated and included in the equation. The original derivation was for constant depth only; later, Mei and Meháute (1966) and shortly afterwards Peregrine (1967))derived Boussinesq equations for variable depth. While Mei and Meháute chose the velocity at the bottom as the dependent variable, Peregrine used the depth-averaged velocity. Due to the wide popularity of the equations derived by Peregrine, these equations are often referred to as the standard Boussinesq equations for variable depth in coastal engineering community.

The standard Boussinesq equations are valid only for relatively small kh and H/h values where kh and H/h represents the parameters indicating the relative depth (dispersion) and the wave steepness (nonlinearity), respectively. Witting (1984) made the first attempt to improve the dispersion characteristics of a 1-D

Boussinesq-like model. Madsen et al. (1991) and Madsen and Sørensen (1992) included higher order terms with adjustable coefficients into the standard Boussinesq equations for constant and variable water depth, respectively. Beji and Nadaoka (1996) gave an alternative derivation of Madsen and Sørensen (1992) Boussinesq equations with Padé (2,2).

Liu and Wu (2004) presented a highly nonlinear Boussines model with specific applications to ship waves generated by a moving pressure distribution in a rectangular and trapezoidal channel. Torsvik et al. (2009b) made a numerical investigation on waves generated by a pressure disturbance moving at constant speed in a channel with a variable cross-channel depth profile by using Lynett et al. (2002) and Liu and Wu's (2004) COULWAVE long wave model. Torsvik et al. (2009a) also applied their model to simulate nonlinear waves generated by fast ferries. Nascimento et al. (2009) adapted Wei and Kirby's (1995) FUNWAVE in order to include a specified moving pressure at the free surface. All these works use the same type of cosine function to represent the moving surface object. In this paper, besides a relatively simple hemispherical shape, a paraboloid-like function is used to model a moving ship in a more refined form.

The numerical model with moving pressure field is first tested for 1-D case. The analytical solutions as obtained from the linearized 1-D long wave equations for a Gaussian-shaped moving surface pressure are compared with the numerical results of the scheme.

For 2-D case the symmetrical accuracy of the model is ascertained first by performing a ring test. Afterwards, waves generated by a moving hemispherical pressure field are simulated. Then, the numerical simulations performed for the slender shiplike surface pressure distribution are used for comparing the wedge

* Corresponding author. Tel.: +90 212 285 64 18.
E-mail address: bayraktard@itu.edu.tr (D. Bayraktar Ersan).

angles with their analytical counterparts as given by Havelock (1908) according to a linearized theory.

Finally the effects of nonlinearity on the generated wave patterns are examined for a selected case by running the numerical scheme in linearized mode and in the nonlinear mode, separately.

2. Boussinesq equations with improved dispersion characteristics

Dispersion relation of Peregrine's (1967) model is an accurate approximation to Stokes first-order wave theory for relatively small values of the dispersion parameter μ. Madsen et al. (1991) improved the dispersion characteristics of this system by adding extra dispersive terms to the momentum equations as expressed in terms of depth-integrated velocities. The form of the dispersion relation is determined by specifying a free parameter according to a preferred approach, which may be an error minimization procedure or matching with the Padé expansion of linear theory dispersion relation. Compared to the classical Boussinesq equations the improved equations contain extra dispersive terms, which enables them to simulate relatively shorter waves with better accuracy. Later, this procedure has been extended to the case of variable depth by Madsen and Sørensen (1992). Alternatively, Beji and Nadaoka (1996) introduced a slightly different method to improve the dispersion characteristics by a simple algebraic manipulation of Peregrine's work for variable depth.

In this work, Boussinesq equations as derived by Beji and Nadaoka (1996) are used with the addition of a pressure gradient to the momentum equation:

$$\mathbf{u}_t + (\mathbf{u} \cdot \nabla)\mathbf{u} + g\nabla\eta = (1+\beta)\frac{h}{2}\nabla[\nabla \cdot (h\mathbf{u}_t)] + \beta g\frac{h}{2}\nabla[\nabla \cdot (h\nabla\eta)]$$
$$-(1+\beta)\frac{h^2}{6}\nabla(\nabla \cdot \mathbf{u}_t) - \beta g\frac{h^2}{6}\nabla(\nabla^2\eta) + \frac{\nabla p}{\rho} \quad (1)$$

$$\frac{\partial\eta}{\partial t} + \nabla \cdot [(h+\eta)\mathbf{u}] = 0 \quad (2)$$

where $\mathbf{u}$ is the vertically averaged or mean horizontal velocity vector with components (u,v), and η is the free surface displacement as measured from the still water level. g is the gravitational acceleration and $h = h(x,y)$ is the spatially varying local water depth. Subscript t denotes partial differentiation with respect to time and ∇ is the two-dimensional horizontal gradient operator with components $(\partial/\partial x, \partial/\partial y)$. β is a scalar set to $\beta = 1/5$ according to the second order Padé expansion of the linear theory dispersion relation. Note that $\beta = 0$ corresponds to Peregrine's original equations. When $\beta = 1/5$ the model may propagate relatively shorter waves ($h/\lambda = 1$) with acceptable errors in celerity.

3. Numerical algorithm

3.1. Discretization of governing equations

The governing equations given by Eqs. (1) and (2) are discretized on an Arakawa staggered C-grid system as shown in Fig. 1.

In the discretization process the continuity equation is embedded into the momentum equation in a manner first used by O'Brien and Hurlburt (1972) for the solution of two-layer shallow water equations. Such an arrangement enables running the long wave mode in the implicit formulation of the Boussinesq mode. Accordingly, the continuity equation is discretized as

$$\frac{\eta_{i,j}^{k+1} - \eta_{i,j}^k}{\Delta t} + \frac{1}{2}h\left[\left(\frac{\partial u}{\partial x}\right)^{k+1} + \left(\frac{\partial u}{\partial x}\right)^k\right]_{i-1/2,j}$$
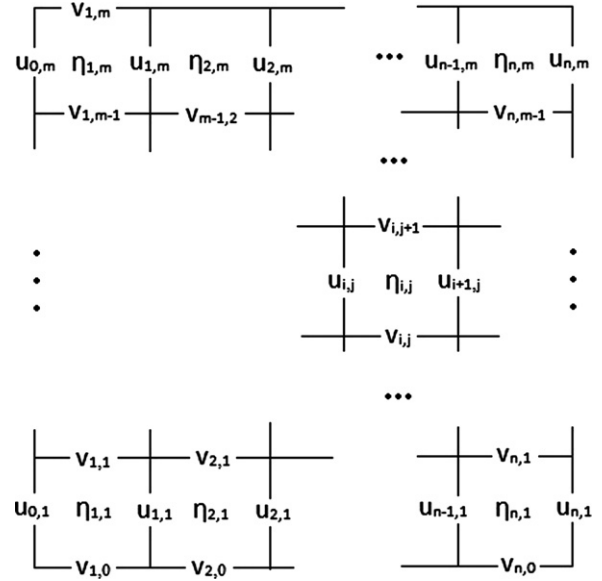

Fig. 1. Location of dependent in Arakawa staggered C-grid system.

$$= -\left[h_x u_{i-1/2,j}^{k+1/2} + h_y v_{i,j-1/2}^{k+1/2} + \frac{\partial}{\partial x}(\eta u)^{k+1/2} + \frac{\partial}{\partial y}(\eta v)^{k+1/2} + h\frac{\partial v_{i,j-1/2}^{k+1/2}}{\partial y}\right]$$
$$(3)$$

where i and j denotes the spatial time steps in the x- and y-directions while k indicates the time level. Multiplying both sides by Δt and differentiating with respect to x gives

$$\left(\frac{\partial\eta}{\partial x}\right)_{i,j}^{k+1} = \left(\frac{\partial\eta}{\partial x}\right)_{i,j}^k - \frac{1}{2}h\left[\left(\frac{\partial^2 u}{\partial x^2}\right)^{k+1} + \left(\frac{\partial^2 u}{\partial x^2}\right)^k\right]_{i-1/2,j}\Delta t$$
$$-2h_x\left(\frac{\partial u}{\partial x}\right)_{i-1/2,j}^{k+1/2}\Delta t - h_y\left(\frac{\partial v}{\partial x}\right)_{i,j-1/2}^{k+1/2}\Delta t$$
$$-h_x\left(\frac{\partial v}{\partial y}\right)_{i,j-1/2}^{k+1/2} - h\left(\frac{\partial^2 v}{\partial x\partial y}\right)_{i,j-1/2}^{k+1/2}\Delta t$$
$$-\frac{\partial^2}{\partial x^2}(\eta u)_{i-1/2,j}^{k+1/2}\Delta t - \frac{\partial^2}{\partial x\partial y}(\eta v)_{i,j-1/2}^{k+1/2}\Delta t \quad (4)$$

Likewise, multiplying Eq. (3) by Δt and differentiating with respect to y gives

$$\left(\frac{\partial\eta}{\partial y}\right)_{i,j}^{k+1} = \left(\frac{\partial\eta}{\partial y}\right)_{i,j}^k - \frac{1}{2}h\left[\left(\frac{\partial^2 v}{\partial y^2}\right)^{k+1} + \left(\frac{\partial^2 v}{\partial y^2}\right)^k\right]_{i-1/2,j}\Delta t$$
$$-2h_y\left(\frac{\partial v}{\partial y}\right)_{i-1/2,j}^{k+1/2}\Delta t - h_x\left(\frac{\partial u}{\partial y}\right)_{i,j-1/2}^{k+1/2}\Delta t$$
$$-h_y\left(\frac{\partial u}{\partial x}\right)_{i,j-1/2}^{k+1/2}\Delta t - h\left(\frac{\partial^2 u}{\partial x\partial y}\right)_{i,j-1/2}^{k+1/2}\Delta t$$
$$-\frac{\partial^2}{\partial x\partial y}(\eta u)_{i-1/2,j}^{k+1/2}\Delta t - \frac{\partial^2}{\partial y^2}(\eta v)_{i,j-1/2}^{k+1/2}\Delta t \quad (5)$$

Eqs. (4) and (5) are to be used in the discretized forms of the x- and y-components of the momentum equation, respectively. The x-component of the momentum equation is discretized as

$$\frac{u_{i,j}^{k+1} - u_{i,j}^k}{\Delta t} + \frac{1}{2}g\left[\left(\frac{\partial\eta}{\partial x}\right)^{k+1} + \left(\frac{\partial\eta}{\partial x}\right)^k\right]_{i+1/2,j}$$
$$= (1+\beta)\frac{h^2}{3}\left[\left(\frac{\partial^2 u}{\partial x^2}\right)^{k+1} - \left(\frac{\partial^2 u}{\partial x^2}\right)^k\right]\frac{1}{\Delta t}$$
$$+(1+\beta)hh_x\left[\left(\frac{\partial u}{\partial x}\right)^{k+1} - \left(\frac{\partial u}{\partial x}\right)^k\right]\frac{1}{\Delta t} - (uu_x)^{k+1/2} - (vu_y)^{k+1/2}$$

$$+(1+\beta)\frac{h^2}{3}v_{xyt}+\frac{1}{2}(1+\beta)hh_xv_{yt}+\frac{1}{2}(1+\beta)hh_yv_{xt}$$

$$+g\beta\frac{h^2}{3}\eta_{xxx}+g\beta hh_x\eta_{xx}+g\beta\frac{h^2}{3}\eta_{xyy}$$

$$+\frac{1}{2}g\beta hh_x\eta_{yy}+\frac{1}{2}g\beta hh_y\eta_{xy}-\frac{1}{\rho}p_x \tag{6}$$

where the terms given in undiscretized form are to be discretized according to the Arakawa C-grid system at time level $k+1/2$. Substituting $(\partial\eta/\partial x)_{i,j}^{k+1}$ as given in Eq. (4) into the above equation, multiplying by Δt and rearranging gives

$$h\left[\frac{1}{3}(1+\beta)h+\frac{1}{4}g\Delta t^2\right]\left(\frac{\partial^2 u}{\partial x^2}\right)^{k+1}+h_x\left[(1+\beta)h+\frac{1}{2}g\Delta t^2\right]\left(\frac{\partial u}{\partial x}\right)^{k+1}-u_{i,j}^{k+1}$$

$$=h\left[\frac{1}{3}(1+\beta)h-\frac{1}{4}g\Delta t^2\right]\left(\frac{\partial^2 u}{\partial x^2}\right)^k+h_x\left[(1+\beta)h-\frac{1}{2}g\Delta t^2\right]\left(\frac{\partial u}{\partial x}\right)^k$$

$$-u_{i,j}^k+g\left(\frac{\partial\eta}{\partial x}\right)^k\Delta t-\frac{1}{2}h_x\left[(1+\beta)h+\frac{1}{2}g\Delta t^2\right]\left(\frac{\partial v}{\partial y}\right)^{k+1}$$

$$+\frac{1}{2}h_x\left[(1+\beta)h-\frac{1}{2}g\Delta t^2\right]\left(\frac{\partial v}{\partial y}\right)^k-\frac{1}{2}h_y\left[(1+\beta)h+\frac{1}{2}g\Delta t^2\right]\left(\frac{\partial v}{\partial x}\right)^{k+1}$$

$$+\frac{1}{2}h_y\left[(1+\beta)h-\frac{1}{2}g\Delta t^2\right]\left(\frac{\partial v}{\partial x}\right)^k-h\left[\frac{1}{3}(1+\beta)h+\frac{1}{4}g\Delta t^2\right]\left(\frac{\partial^2 v}{\partial x\partial y}\right)^{k+1}$$

$$+h\left[\frac{1}{3}(1+\beta)h-\frac{1}{4}g\Delta t^2\right]\left(\frac{\partial^2 v}{\partial x\partial y}\right)^k+[(uu_x)^{k+1/2}+(vu_y)^{k+1/2}]\Delta t$$

$$-g\beta h\Delta t\left[\frac{h}{3}(\eta_{xxx}+\eta_{xyy})+h_x\left(\eta_{xx}+\frac{1}{2}\eta_{yy}\right)+\frac{1}{2}h_y\eta_{xy}\right]$$

$$-\frac{1}{2}g\Delta t^2\left[\frac{\partial^2}{\partial x^2}(\eta u)^{k+1/2}+\frac{\partial^2}{\partial x\partial y}(\eta v)^{k+1/2}\right]-\frac{1}{\rho}p_x\Delta t \tag{7}$$

The y-momentum equation is discretized likewise

$$h\left[\frac{1}{3}(1+\beta)h+\frac{1}{4}g\Delta t^2\right]\left(\frac{\partial^2 v}{\partial y^2}\right)^{k+1}+h_y\left[(1+\beta)h+\frac{1}{2}g\Delta t^2\right]\left(\frac{\partial v}{\partial y}\right)^{k+1}-v_{i,j}^{k+1}$$

$$=h\left[\frac{1}{3}(1+\beta)h-\frac{1}{4}g\Delta t^2\right]\left(\frac{\partial^2 v}{\partial y^2}\right)+h_y\left[(1+\beta)h-\frac{1}{2}g\Delta t^2\right]\left(\frac{\partial v}{\partial y}\right)^k$$

$$-v_{i,j}^k+g\left(\frac{\partial\eta}{\partial x}\right)^k\Delta t-\frac{1}{2}h_y\left[(1+\beta)h+\frac{1}{2}g\Delta t^2\right]\left(\frac{\partial u}{\partial x}\right)^{k+1}$$

$$+\frac{1}{2}h_y\left[(1+\beta)h-\frac{1}{2}g\Delta t^2\right]\left(\frac{\partial u}{\partial x}\right)^k-\frac{1}{2}h_x\left[(1+\beta)h+\frac{1}{2}g\Delta t^2\right]\left(\frac{\partial u}{\partial y}\right)^{k+1}$$

$$+\frac{1}{2}h_x\left[(1+\beta)h-\frac{1}{2}g\Delta t^2\right]\left(\frac{\partial u}{\partial y}\right)^k-h\left[\frac{1}{3}(1+\beta)h+\frac{1}{4}g\Delta t^2\right]\left(\frac{\partial^2 u}{\partial x\partial y}\right)^{k+1}$$

$$+h\left[\frac{1}{3}(1+\beta)h-\frac{1}{4}g\Delta t^2\right]\left(\frac{\partial^2 u}{\partial x\partial y}\right)^k+[(uv_x)^{k+1/2}+(vv_y)^{k+1/2}]\Delta t$$

$$-g\beta h\Delta t\left[\frac{h}{3}(\eta_{yyy}+\eta_{xxy})+h_y\left(\eta_{yy}+\frac{1}{2}\eta_{xx}\right)+\frac{1}{2}h_x\eta_{xy}\right]$$

$$-\frac{1}{2}g\Delta t^2\left[\frac{\partial^2}{\partial y^2}(\eta v)^{k+1/2}+\frac{\partial^2}{\partial x\partial y}(\eta u)^{k+1/2}\right]-\frac{1}{\rho}p_y\Delta t \tag{8}$$

Note that all the time derivatives are centered at time level $k+1/2$ as the spatial derivatives are evaluated at $k+1/2$ by averaging the derivatives at time levels k and $k+1$. Since all the spatial derivatives are also centered, the scheme is fully centered and accurate to the second order in both time and space. The numerical solution proceeds as follows. First, the provisional values of η are computed from the continuity equation (3) using the old time velocity values. The discretized x- and y-momentum equations (7) and (8) yield a tridiagonal matrix system for the velocities u and v at new time level. For the x-sweep, the new time level values v^{k+1}s are treated as known by using the last computed values so that u^{k+1}s are the only unknowns. The resulting matrix system is solved by Thomas Algorithm. Similarly for the y-sweep, the v^{k+1}s are the only unknowns to be solved. Finally the continuity equation (3) is used again to obtain the improved values of η using the newly computed u^{k+1} and v^{k+1} values. At each time step the procedure is iterated thrice, which is found to be sufficient for reliable results. For a more precise approach the successive values of the variables may be compared according to a convergence criterium. Nevertheless the numerical experiments do not justify the additional computational load as no appreciable improvement in the results is observed with increasing iteration number.
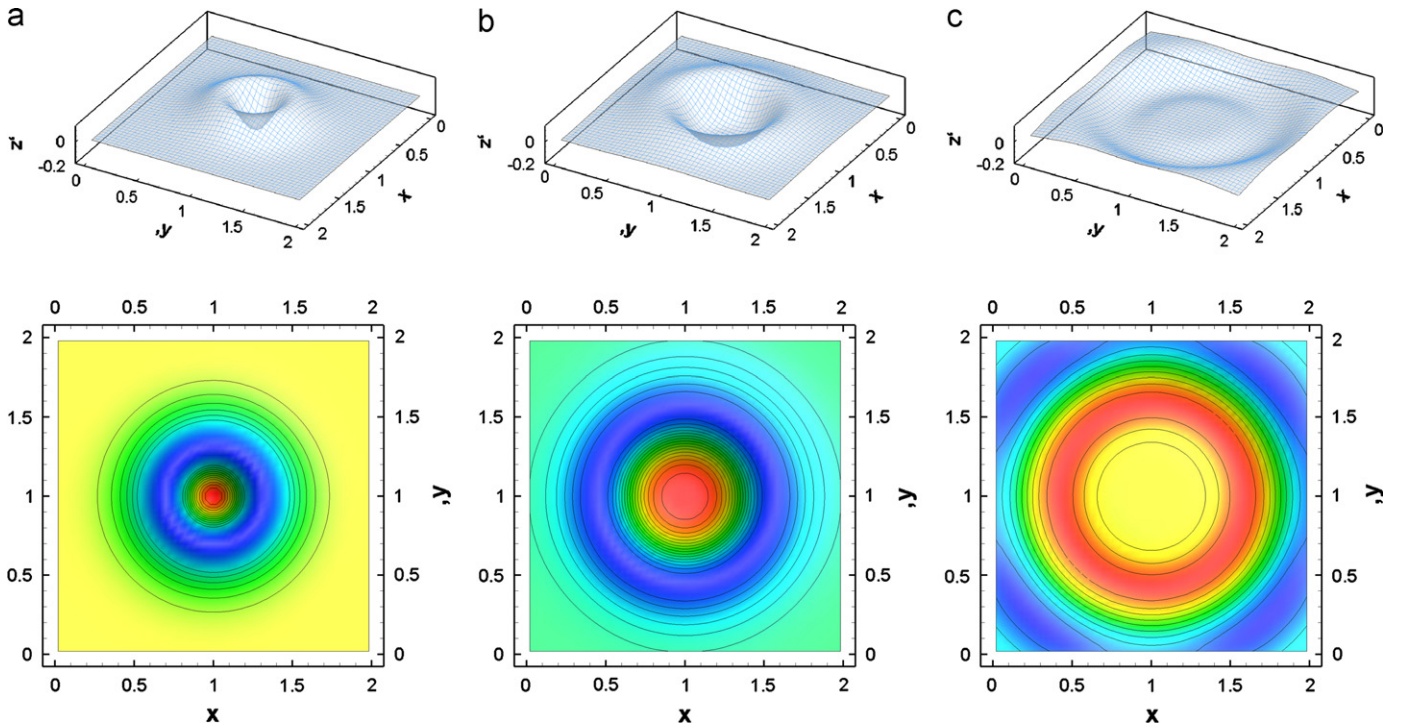

Fig. 2. Ring test for 2-D Boussinesq equations with $\beta=1/5$ at $t=0.25$ (a), $t=0.5$ (b) and $t=1.0$ s (c). Upper row: perspective views, lower row: contour graphics.

3.2. Boundary conditions

All the boundaries are specified as the radiation type boundary, across which the waves leave the domain without any hinderance. For one dimensional waves Sommerfeld radiation condition reads for u and v, respectively:

$$u_t + c_x u_x = 0$$
$$v_t + c_y v_y = 0 \qquad (9)$$

where c_x and c_y denote the x- and y-components of the phase celerity c. Numerical determination of c_x and c_y at every time step requires the computation of the incident wave angle hence is not quite reliable. Therefore, as is usually done, c is used for both directions and c is computed according to the dispersion relationship of the improved Boussinesq equations for the local water depth. Higher-order boundary conditions as given by Engquist and Majda (1977) may be used; however, the simpler Sommerfeld radiation condition with constant c for both directions is found to be acceptable enough as observed in the ring test.

4. Test cases for verification of numerical scheme

4.1. Ring test

The performance of the non-reflective boundaries is checked by a ring test which reveals the symmetrical accuracy of the model. The ring tests for all the modes (long wave, classical Boussinesq and Boussinesq with Padé (2,2)) of the numerical scheme are

performed; however, only the test for the improved Boussinesq model is shown here. The computational domain is taken as 2×2 m with $h = 1$ m water depth. The region is discretized by 50 points along both x- and y-axes. Time step $\Delta t = 1/40$ s and the simulations are shown for $t = 0.25$ s, 0.5 s and 1.0 s in Fig. 2. The contour plots show nearly perfect symmetry.

4.2. A 1-D moving pressure test

For testing the accuracy of numerically simulated waves due to a moving pressure field, a 1-D case with known analytical solution is considered. The analytical solution for the 1-D linearized long wave equations is recapitulated first and then comparisons with the numerical solutions are given. The linearized long wave equations for constant depth may be written as

$$\eta_t + h u_x = 0$$
$$u_t + g \eta_x = -\frac{1}{\rho} p_x \qquad (10)$$

where p is the applied surface pressure. In absence of any forcing function ($p = 0$) the above equations have the free wave solutions $\eta_1 = a_1 f(x-ct)$, $\eta_2 = a_2 f(x+ct)$ and $u_1 = (c/h)a_1 f(x-ct)$, $u_2 = -(c/h) a_2 f(x+ct)$ where $f(x,t)$ is an arbitrary function, a_1 and a_2 are arbitrary constants and $c = \sqrt{gh}$ is the shallow water wave celerity. If the pressure field is defined as $p = p_0 f(x-vt)$ with v being the speed of the pressure field in the positive x-direction then the forced system has a solution of the form $\eta_3 = a_3 f(x-vt)$ and $u_3 = b_3 f(x-vt)$ with a_3 and b_3 to be determined from the wave
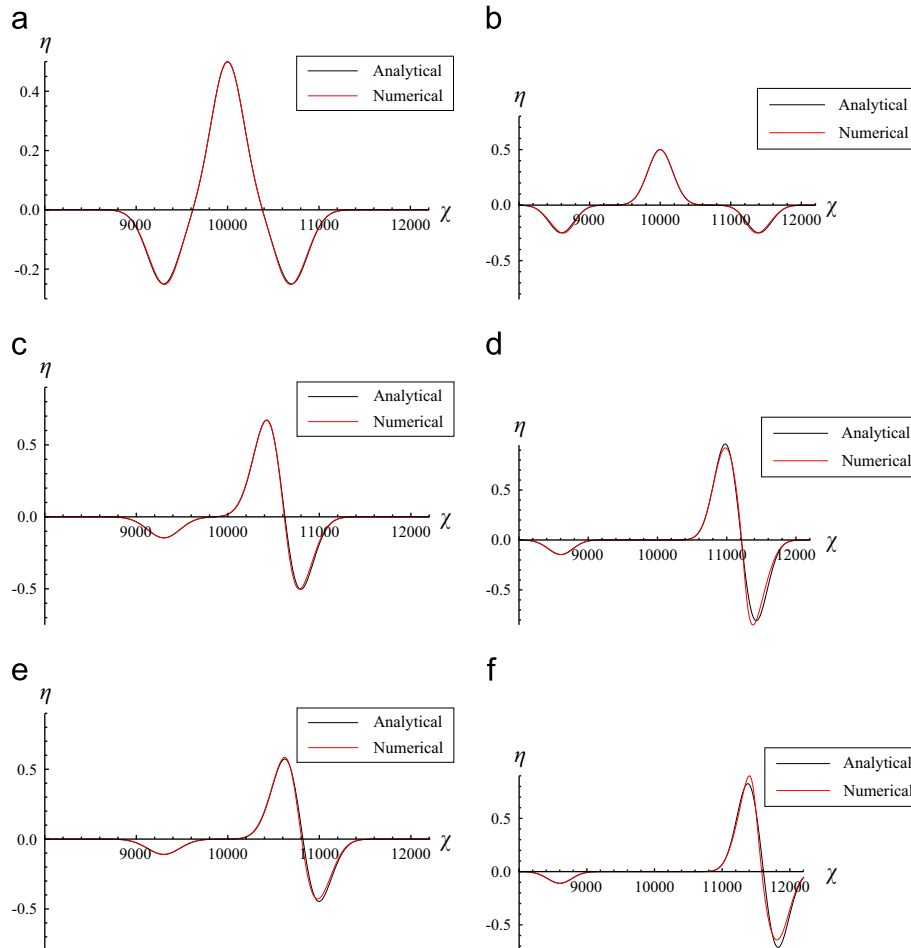

Fig. 3. Comparison of numerical and analytical solutions of linear shallow water wave equations for a moving pressure with $v = 0$ m/s, $v = 10$ m/s and $v = 18$ m/s at $t = 50$ s (left column) and $t = 100$ s (right column): (a) $t = 50$ s, $v = 0$ m/s; (b) $t = 100$ s, $v = 0$ m/s; (c) $t = 50$ s, $v = 10$ m/s; (d) $t = 100$ s, $v = 10$ m/s; (e) $t = 50$ s, $v = 18$ m/s; (f) $t = 100$ s, $v = 18$ m/s.

equations. Substituting η_3, u_3 and p into Eq. (10) gives $a_3 = -hp_0/\rho(c^2-v^2)$ and $b_3 = -vp_0/\rho(c^2-v^2)$. Finally, applying the initial condition that the total displacement and velocity must separately be zero at $t=0$:

$$\eta_1+\eta_2+\eta_3 = 0$$
$$u_1+u_2+u_3 = 0 \tag{11}$$

gives for $a_1 = (c+v)hp_0/2\rho c(c^2-v^2)$ and $a_2 = (c-v)hp_0/2\rho c(c^2-v^2)$. The final solution is then

$$\eta = \frac{hp_0}{2\rho c(c^2-v^2)}[(c+v)f(x-ct)+(c-v)f(x+ct)-2cf(x-vt)] \tag{12}$$

and

$$u = \frac{p_0}{2\rho(c^2-v^2)}[(c+v)f(x-ct)-(c-v)f(x+ct)-2vf(x-vt)] \tag{13}$$

Note that when $t=0$ both η and u become identically zero. For the test case the pressure function f is selected as $f(\chi) = \exp[-(\chi/250)^2]$ where $\chi = x-vt$. $p_0 = -5000$ Pa, $\rho = 1000$ kg/m³, $g=9.81$ m/s² and the water depth is $h=20$ m so that $c = \sqrt{gh} = 14$ m/s. The length of the computational domain is 20 000 m, grid size 20 m and time step 1 s. The initial location of the pressure field is in the middle of the computational domain, $x_0 = 10\,000$ m. Fig. 3 compares the analytical solution with the numerical solution of long wave equations for $v=0$, 10, and 18 m/s cases, which corresponds to the depth-based Froude numbers $Fr = v/c = v/\sqrt{gh} = 0.0$, 0.7, and 1.3 approximately. The same comparisons using the Boussinesq equations with $\beta = 1/5$ instead of the long wave equations are made in Fig. 4. As seen from the figures numerical simulations in both cases agree well with the analytical solution derived from the linearized long wave equations.

Having thus established a certain degree of confidence in the numerical scheme regarding the simulation of surface-forced waves the scheme is now used for 2-D simulations.

5. 2-D numerical simulations

2-D simulations of waves generated by moving pressure fields are performed for two different surface pressure functions; a hemispherical pressure field and a slender-body type pressure field.
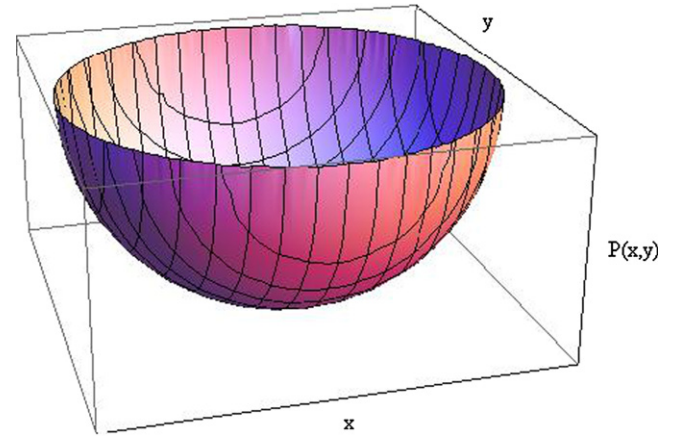

Fig. 5. Definition of the pressure distribution $p(x,y) = p_0\sqrt{1-(x^2+y^2)/R^2}$.
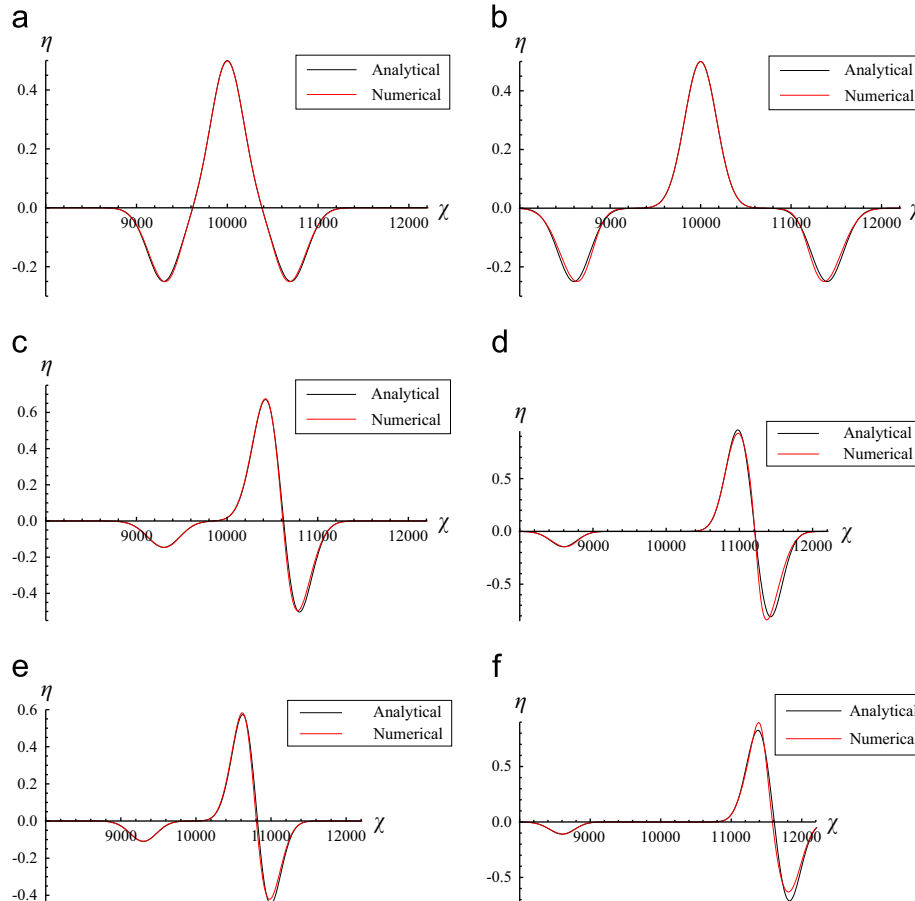

Fig. 4. Comparison of analytical solution with linear shallow water waves and 1-D Boussinesq solution generated by a moving pressure with $v=0$ m/s, $v=10$ m/s and $v=18$ m/s for $\beta=1/5$ at $t=50$ s (left column) and $t=100$ s (right column): (a) $t=50$ s, $v=0$ m/s; (b) $t=100$ s, $v=0$ m/s; (c) $t=50$ s, $v=10$ m/s; (d) $t=100$ s, $v=10$ m/s; (e) $t=50$ s, $v=18$ m/s; (f) $t=100$ s, $v=18$ m/s.

5.1. Hemispherical pressure forcing

A hemispherical pressure field of the form:

$$p(x,y) = p_0\sqrt{1-(x^2+y^2)/R^2} \qquad (14)$$

is used for the first simulation. Here p_0 is the peak value of the pressure distribution, which is attained at $x=0$, $y=0$, and R is the radius of the hemisphere. Fig. 5 shows the hemispherical field.

In the simulation R is taken as 40 m, $p_0 = 300$ Pa and the water depth $h=10$ m which gives $c = \sqrt{gh} = 10$ m/s. The simulation region is 600 m × 300 m with $\Delta x = \Delta y = 2$ m. Time step is taken as $\Delta t = 0.2$ s. In the x-momentum equation $p_x = -xp_0/R^2 [1-(x^2+y^2)/R^2]^{1/2}$ and in the y-momentum $p_y = -yp_0/R^2[1-(x^2+y^2)/R^2]^{1/2}$. Fig. 6
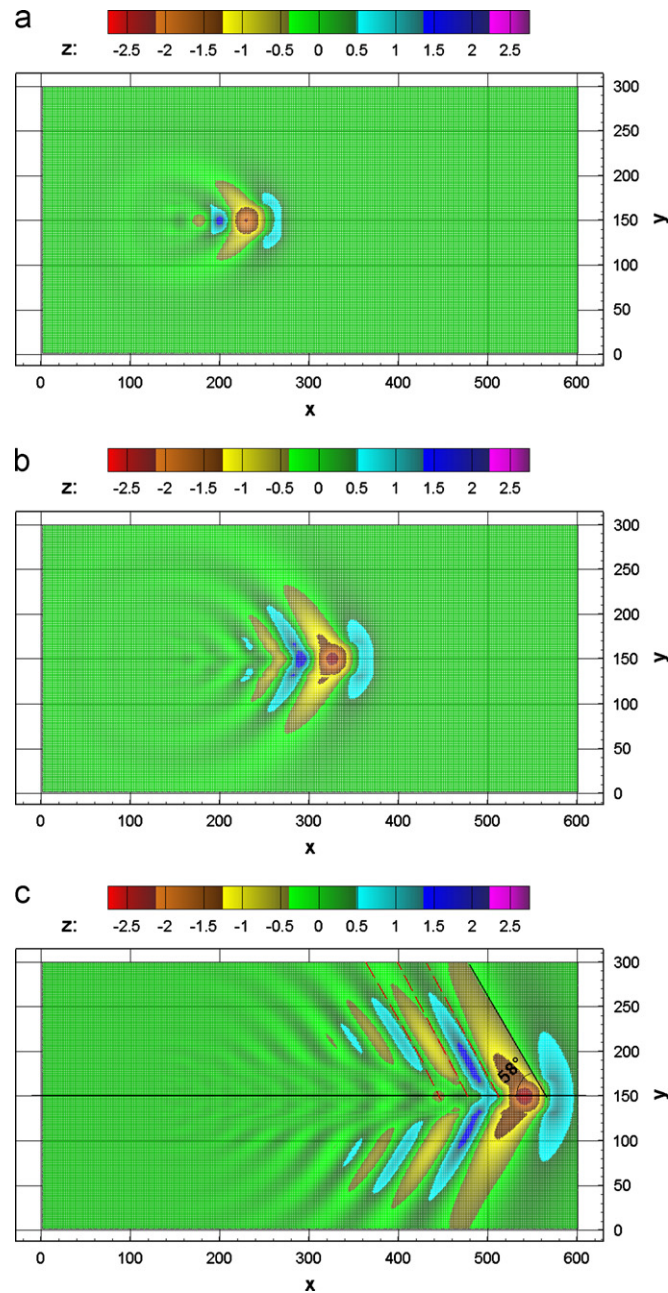

Fig. 6. Wave contours of a moving hemisphere at different time steps using Boussinesq model with $\beta = 1/5$ for $Fr=0.99$: (a) $t=10$ s, $Fr=0.99$; (b) $t=20$ s, $Fr=0.99$; (c) $t=48$ s, $Fr=0.99$.

shows the contour plots of the simulated wave field at $t=10$ s, 20 s and 48 s for the depth-based Froude number $Fr = v/c = v/\sqrt{gh} = 0.99$, which corresponds the pressure field speed $v = 0.99\sqrt{gh} = 0.99c = 9.9$ m/s. It is to be noted that the wedge angle 58° measured from the simulated wave field at $t=48$ s is an acceptable approximation to the theoretical value 51° of Havelock (1908) as can be seen in Table 1 and Fig. 10 of Section 5.2.

5.2. Slender-body type pressure forcing

For a more ship-like form a slender shaped pressure field of the form:

$$p(x,y) = p_0[1-c_L(x/L)^4][1-c_B(y/B)^2]\exp[-a(y/B)^2] \qquad (15)$$

is used. Here p_0 is the peak pressure value which is set to 3000 Pa, which is attained at $x=0$, $y=0$, L is the length-wise, B is the breadth-wise parameter and a, c_B, c_L are shape constants which are set to 16, 2, and 16, respectively. The pressure field $p(x,y)$ is defined only within the intervals $-L/2 \le x \le L/2$ and $-B/2 \le y \le B/2$ and set to zero outside these regions. Fig. 7 shows the slender parabolic type pressure field.

The simulation area is 600 m × 300 m with grid sizes of $\Delta x = \Delta y = 1$ m and the time step $\Delta t = 0.06$ s. In the simulations the length to beam ratio L/B is set to 5 with $L=100$ m and $B=20$ m and the water depth is $h=20$ m, resulting in $c = \sqrt{gh} = 14$ m/s. Note that in the x-momentum equation $p_x = -4p_0(c_L/L)(x/L)^3(1-c_B (y/B)^2)e^{-a(y/B)^2}$ and in the y-momentum equation $p_y = -2p_0(a/B)[1-c_L(x/L)^4][(c_B/a)+1-c_B(y/B)^2](y/B)e^{-a(y/B)^2}$. Unlike the previous

Table 1
Comparisons of numerically obtained wedge angles with Havelock's analytical results for a range of depth-based Froude numbers.

| Fr	Wedge angle		
	Boussinesq (numerical)	Havelock (analytical)	Relative error percentage (%)
0.63	18	19.69	8.58
0.70	20	20.26	1.29
0.75	21	21.10	0.47
0.86	26	25.36	2.51
0.90	25	28.50	12.28
0.96	35	37.78	7.37
0.97	44	40.69	8.14
0.98	51	44.66	14.18
0.99	54	51.01	5.86
1.01	82	81.93	0.08
1.05	72	72.25	0.34
1.10	64	65.38	2.11
1.20	57	56.44	0.99
1.30	51	50.28	1.42
1.40	44	45.58	3.48
1.50	41	41.81	1.94
1.70	37	36.03	2.69
1.80	33	33.75	2.22
2.00	30	30.00	0.00
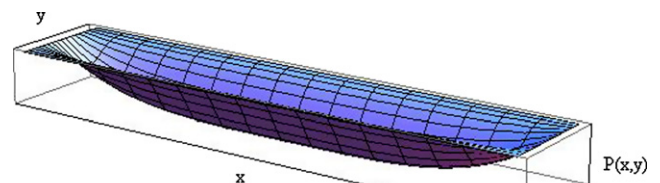
Fig. 7. Perspective view of the slender-body type pressure distribution.

test case, a range of depth-based Froude numbers is covered. Out of 19 test cases the contour plots of only three cases, corresponding to $Fr=0.98$ and 1.30 are shown in Figs. 8 and 9.

Havelock (1908) investigated the wave patterns due to a moving surface pressure and showed the main differences between subcritical and supercritical Froude numbers. The results for the wedge and propagation angles show that as the Froude number decreases the divergent waves become more dominant while transverse wave's position, whether being crest or trough, changes with respect to ship velocity. For the wedge angle of a point impulse moving on water of finite depth Havelock gives

$$\alpha = \arccos \sqrt{8(1-n)}/(3-n) \quad \text{if } Fr \leq 1$$

$$\alpha = \arcsin \sqrt{p} \quad \text{if } Fr > 1$$

where $p = gh/v^2 = c^2/v^2 = 1/Fr^2$. For a given Froude number or p in the subcritical range, first kh is solved by iteration from the relationship $m(3-n) = 2/p$ where $m = \tanh kh/kh$ and $n = 2kh/\sinh 2kh$. Afterwards, using the computed kh the numerical value of n is obtained to compute α. For the supercritical range α is a function of p alone therefore no additional computation is needed. The tabular form of the numerically and analytically computed wedge angles for the Froude numbers considered is given in Table 1. It should be mentioned that some limited number of numerical values given by Havelock does not exactly match with their counterparts in Table 1, as the present table is compiled by high-accuracy computations.

It is to be noted that in the subcritical range as Froude number approaches zero the relative depth kh becomes larger. On the other hand, in the entire supercritical range kh assumes the limiting case
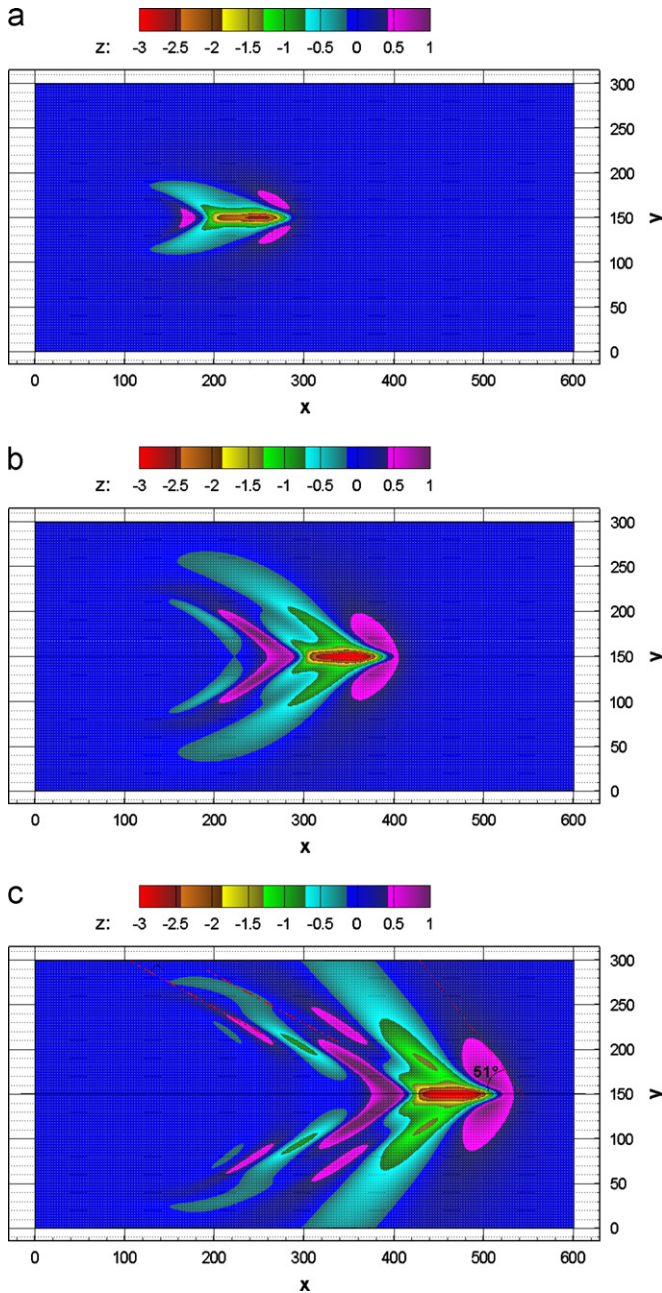
Fig. 8. Wave contours generated by a slender-body type moving pressure field using Boussinesq model with $\beta = 1/5$ for $Fr=0.98$: (a) $t=7.2$ s, $Fr=0.98$; (b) $t=15$ s, $Fr=0.98$; (c) $t=24$ s, $Fr=0.98$.
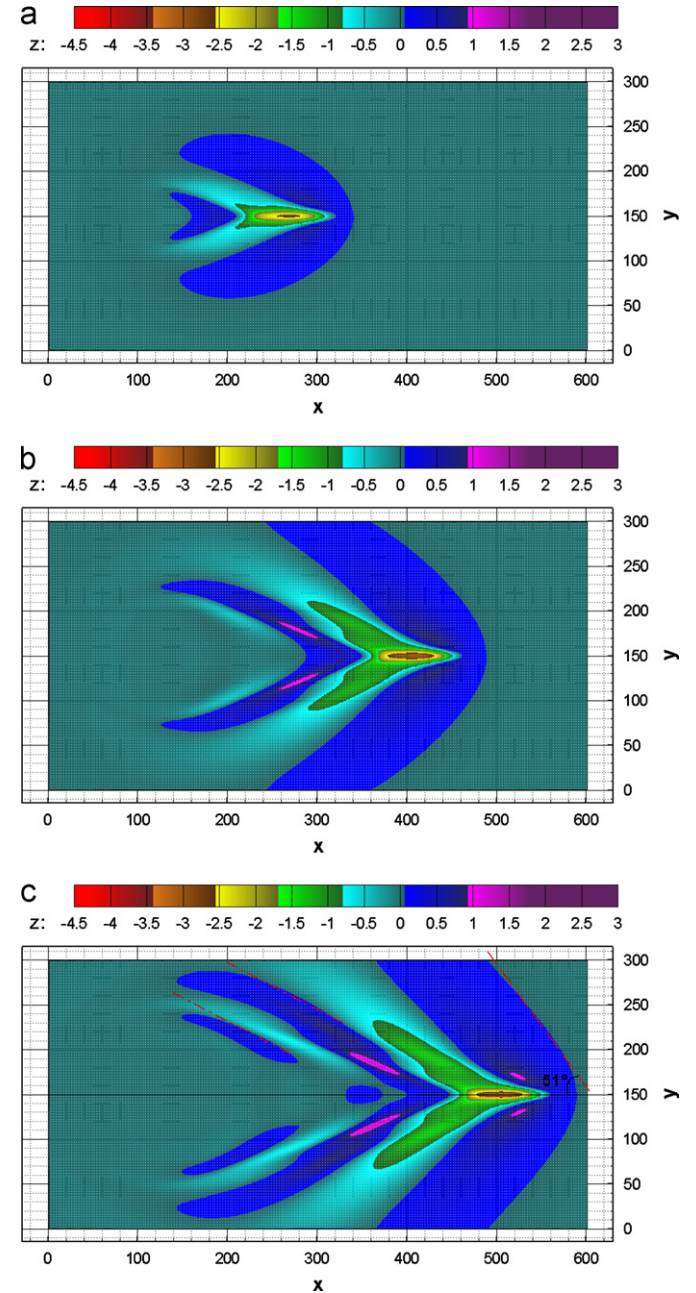
Fig. 9. Wave contours generated by a slender-body type moving pressure field using Boussinesq model with $\beta = 1/5$ for $Fr=1.3$: (a) $t=7.2$ s, $Fr=1.3$; (b) $t=15$ s, $Fr=1.3$; (c) $t=24$ s, $Fr=1.3$.

of zero and disappears from the wedge angle computations. Thus, in a sense, low Froude numbers represent relatively deep waters while high Froude numbers correspond to very shallow waters. For $Fr = 0$ Kelvin's well-known result of a deep-water wedge angle $\alpha = 19°28'$ is obtained as may be seen in Fig. 10 where the wedge angles computed from Havelock's analytical formulas and measured from the graphs of the numerical solutions of the present Boussinesq model are shown.

Finally, two perspective views of a nonlinear simulation with slender-body shaped pressure field for $Fr = 0.9$ are shown in Fig. 11. The nonlinearity is ascertained by considerably increased pressure amplitude p_0 (twice the previous simulations in Section 5.2). Nevertheless, no appreciable differences are observed in the wedge angles for the simulation shown here and for the other simulations not shown. The nonlinearity appears to affect the vertical symmetry of the wave profile only. Otherwise, the essential characteristics of the wave pattern remain nearly the same.
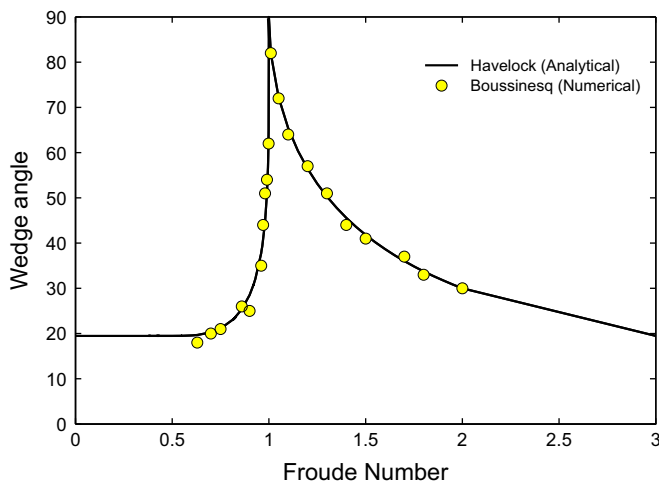

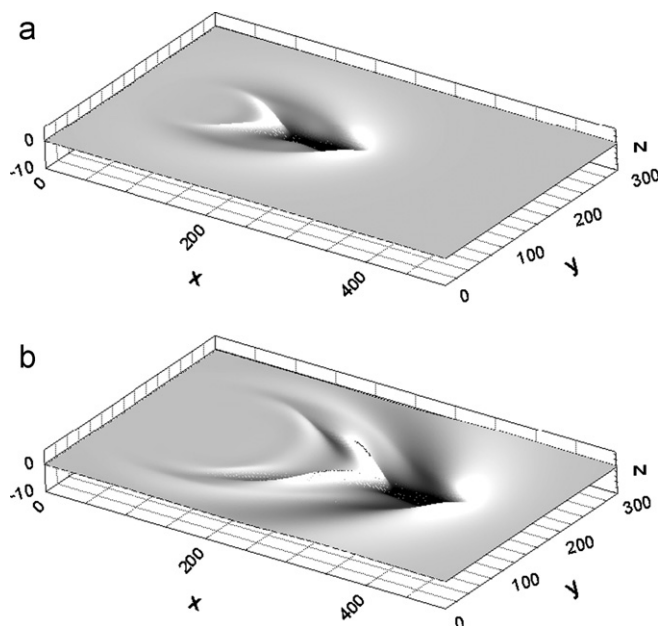**Fig. 10.** Comparison of numerically obtained wedge angles with Havelock's theoretical formulas.

6. Conclusion

Several types of Boussinesq equations are in use for modeling nearshore waves or waves in intermediate water depths. Besides these rather common applications, the Boussinesq equations may also be employed to model wave generation and propagation by moving surface disturbances. The surface disturbance may come from a moving free surface object or bottom movement as in the case of underwater earthquakes. The former is associated with a moving surface vessel, which is the main problem investigated in this paper.

By adding a moving surface pressure into Boussinesq equations, the wave patterns for different depth-based Froude numbers are investigated for a hemispherical and for a slender-body type pressure field, respectively. The slender-body type pressure distribution, which represents a ship-like form in a more realistic way, is used for numerical simulation of wave patterns for various Froude numbers. The computed wedge angles are compared with Havelock's (1908) analytical results.

Comparisons reveal good agreement with the theory, especially for supercritical Froude numbers, $Fr \geq 1$, where the relative depth is small. In the subcritical range, $Fr \leq 1$, the average error percentage between the computed and the theoretical values is around 6.5%, considerably greater than those of the supercritical range, which is on the average 1.5%. The reason for this asymmetry in average error percentages between sub- and supercritical Froude numbers is probably due to the depth limited character of the Boussinesq equations albeit improved. As indicated before, the subcritical range indicates relatively greater depths with completely deep water for zero Froude number. Therefore, the relatively poor performance of the numerical model in the subcritical range may be attributed to the deep water characteristics of the waves generated. Performance comparisons with 3-D model simulations would clarify this particular point. Nonlinearity appears to play only a relatively minor role by affecting the wave symmetry without altering the overall wave patterns such as the wedge angles as observed from the comparisons of the linear and nonlinear simulations. Finally, applications of the present scheme to study the transformation of ship-wave spectra over mildly varying bathymetry and possible extensions of the equations to strongly varying depths are being planned as future work.

References

Beji, S., Nadaoka, K., 1996. A formal derivation and numerical modelling of the improved Boussinesq equations for varying depth. Ocean Eng. 23, 691–704.

Belibassakis, K.A., 2003. A coupled-mode technique for the transformation of ship-generated waves over variable bathymetry regions. Appl. Ocean Res. 25, 321–336.

Boussinesq, J.V., 1872. Theory of waves and surges which propagate the length of a horizontal rectangular canal, imparting to the fluid contained within the canal velocities that are sensibly the same from the top to the bottom. J. Math. Pures Appl. 17, 55–108.

Engquist, B., Majda, A., 1977. Absorbing boundary conditions for the numerical simulation of waves. Math. Comput. 31, 629–651.

Havelock, T., 1908. The propagation of groups of waves in dispersive media, with application to waves on water produced by a travelling disturbance. Proc. R. Soc. London 81, 398–430.

Fig. 11. Perspective views of nonlinear waves generated by slender-body type moving pressure for $Fr = 0.9$ at $t = 10$ s (a) and $t = 20$ s (b).

Liu, P., Wu, T., 2004. Waves generated by moving pressure disturbances in rectangular and trapezoidal channels. J. Hydraul. Res. 42, 163–171.

Lynett, P., Wu, T., Liu, P., 2002. Modeling wave runup with depth-integrated equations. Coastal Eng. 46, 89–107.

Madsen, P.A., Murray, R., Sørensen, O.R., 1991. A new form of the Boussinesq equations with improved linear dispersion characteristics. Coastal Eng. 15, 371–388.

Madsen, P.A., Sørensen, O.R., 1992. A new form of the Boussinesq equations with improved linear dispersion characteristics. Part 2. A slowly-varying bathymetry. Coastal Eng. 18, 183–204.

Mei, C., Meháute, L., 1966. Note on the equations of long waves over an uneven bottom. J. Geophys. Res. 71, 393.

Nascimento, M.F., Neves, C.F., Maciel, G.d.F., 2009. Propagation of ship waves on a sloping bottom. In: 31st International Conference on Coastal Engineering, Hamburg, Germany, August 31–September 05, 2008, pp. 696–708.

O'Brien, J.J., Hurlburt, H.E., 1972. A numerical model of coastal upwelling. J. Phys. Oceanogr. 2, 14–26.

Peregrine, D.H., 1967. Long waves on a beach. J. Fluid Mech. 27, 815–827.

Torsvik, T., Didenkulova, I., Soomere, T., Parnell, K.E., 2009a. Variability in spatial patterns of long nonlinear waves from fast ferries. Nonlinear Proc. Geophys. 16, 351–363.

Torsvik, T., Pedersen, G., Dysthe, K., 2009b. Waves generated by a pressure disturbance moving in a channel with a variable cross-sectional topography. J. Waterway Port Coast. Ocean Eng. 135, 120–123.

Wei, G., Kirby, J., 1995. Time-dependent numerical code for extended Boussinesq equations. J. Waterway Port Coast. Ocean Eng. 121, 251–261.

Witting, J.M., 1984. A unified model for the evolution nonlinear water waves. J. Comput. Phys. 56, 203–236.